CMS Physics Analysis Summary

Contact: cms-pag-conveners-heavyions@cern.ch 2017/02/07

Measurement of the Skewness of Elliptic Flow Fluctuations in PbPb Collisions at $\sqrt{s_{NN}} = 5.02$ TeV

The CMS Collaboration

Abstract

Event-by-event flow harmonics are studied for PbPb collisions at $\sqrt{s_{NN}} = 5.02$ TeV using the CMS detector at the LHC. Flow harmonic probability distributions $p(v_2)$ are obtained using particles of $0.3 \leq p_T \leq 3.0$ GeV/c and $|\eta| \leq 1.0$ and are unfolded to remove smearing effects from observed azimuthal particle distributions. Cumulant flow harmonics are determined from the moments of $p(v_2)$ and used to estimate the standardized elliptic flow skewness in 5% wide centrality bins up to 60%. Hydrodynamic models predict that flow fluctuations will lead to a non-Gaussian component in the flow distributions with a negative skew with respect to the reaction plane. A significant negative skewness is observed for all centrality bins as evidenced by a splitting between $v_2\{4\}$ and $v_2\{6\}$ cumulants. In addition, elliptic power law distribution fits are made to the $p(v_2)$ distributions to infer information on the nature of initial-state eccentricity distributions. The elliptic power law parametrization is found to provide a more accurate description of the fluctuations than the Bessel-Gaussian parametrization.

1 Introduction

Ultrarelativistic heavy-ion collisions at the Relativistic Heavy Ion Collider (RHIC) and the Large Hadron Collider (LHC) create a hot, dense state of matter that consists of strongly-interacting quarks and gluons, the so-called Quark-Gluon Plasma (QGP) [1–6]. The QGP is found to behave as a nearly perfect fluid with a shear viscosity to entropy density ratio η/s that is on the order of the lowest possible value for a quantum fluid [7]. The fluid-like properties of the QGP are inferred from studies of its collective phenomena, which are described well by hydrodynamic models [8]. Large pressure gradients from strong interactions and subsequent hydrodynamic evolution result in the transfer of asymmetries in the initial-state collision geometry to a final-state anisotropy in momentum space for the emitted particles [9, 10]. While the presence of a non-zero viscosity will degrade the correspondence between initial- and final-state anisotropies [7, 8], studies of the azimuthal anisotropy of outgoing particle densities make it possible to infer properties of the initial state of the medium as well as its transport properties during its time evolution.

Within the Glauber model [11], the initial geometry of the medium can be expressed by a cumulant expansion of the density distribution [12], where amplitudes ε_n and phases Φ_n of the leading terms are given by

$$\varepsilon_1 e^{i\Phi_1} \equiv -\frac{\{r^3 e^{i\varphi}\}}{\{r^3\}}, \quad \varepsilon_2 e^{2i\Phi_1} \equiv -\frac{\{r^2 e^{2i\varphi}\}}{\{r^2\}}, \quad \text{and} \quad \varepsilon_3 e^{3i\Phi_1} \equiv -\frac{\{r^3 e^{3i\varphi}\}}{\{r^3\}}, \tag{1}$$

where the curly brackets denote averages over the transverse plane in a single event. While the overlapping geometry of the two nucleons results in a dominant impact-parameter dependent elliptic ($n = 2$) term for non-central collisions, quantum fluctuations of the transverse geometry of the participant nucleons and their substructures cause eccentricity fluctuations on an event-by-event basis [10, 13, 14].

Anisotropies in the initial-state density distribution can result in an azimuthally anisotropic distribution of outgoing particles, with

$$\begin{aligned} \frac{dN_{ch}}{d\phi} &\propto 1 + 2\sum_{n=1}^{\infty} v_n^{obs} \cos\left[n\left(\phi - \Psi_n^{obs}\right)\right] \\ &= 1 + 2\sum_{n=1}^{\infty}\left(v_{n,x}^{obs}\cos n\phi + v_{n,y}^{obs}\sin n\phi\right). \end{aligned} \tag{2}$$

In the Fourier expansion, v_n^{obs} and Ψ_n^{obs} denote the n^{th} order observed flow harmonic and the event plane angle, respectively. Viscous hydrodynamic calculations suggest that the v_n coefficients scale linearly with ε_n for $n \leq 3$ with proportionality constants that are sensitive to properties of the medium such as the equation of state and η/s [15–17].

For central to mid-central collisions, fluctuations in the participant eccentricity can be described by a two-dimensional (2D) Gaussian function [13], with

$$p\left(\vec{\varepsilon}_n\right) = \frac{1}{2\pi\delta_{\varepsilon_n}^2}\exp\left[-\left(\vec{\varepsilon}_n - \vec{\varepsilon}_n^{RP}\right) / \left(2\delta_{\varepsilon_n}^2\right)\right]. \tag{3}$$

Here $\vec{\varepsilon}_n^{RP}$ represents the underlying eccentricity vector that is associated with the average geometry of the collision in the reaction plane and δ_{ε_n} quantifies the fluctuation induced "width" of the distribution. If the flow response depends linearly on the participant eccentricity, the fluctuations of the flow vectors can be similarly described by a 2D Gaussian, with

$$p\left(\vec{v}_n\right) = \frac{1}{2\pi\delta^2_{\vec{v}_n}} \exp\left[-\left(\vec{v}_n - \vec{v}_n^{RP}\right) / \left(2\delta^2_{\vec{v}_n}\right)\right], \tag{4}$$

where $\vec{v}_n^{RP}$ and $\delta_{\vec{v}_n}$ are flow analogs to the geometry parametrization described in Eq. 3. The probability distribution of the magnitude of flow is obtained by integrating out the ϕ-dependence of Eq. 4 [13, 18], leading to

$$p\left(v_n\right) = \frac{v_n}{\delta^2_{\vec{v}_n}} \exp\left[-\frac{\left(v_n\right)^2 + \left(v_n^{RP}\right)^2}{2\delta^2_{\vec{v}_n}}\right] I_0\left(\frac{v_n v_n^{RP}}{\delta^2_{\vec{v}_n}}\right), \tag{5}$$

where I_0 is the modified Bessel function of the first kind. This functional form is known as a Bessel-Gaussian.

Historically, properties of $p\left(v_n\right)$ have been inferred from studies using event-averaged values. For example, m-particle correlations are commonly used in flow analyses to measure multi-particle cumulants [19–21]. Flow harmonics based on cumulants are calculated by

$$\begin{aligned}
v_n\{2\}^2 &\equiv \langle v_n^2\rangle, \\
v_n\{4\}^4 &\equiv -\langle v_n^4\rangle + 2\langle v_n^2\rangle^2, \\
v_n\{6\}^6 &\equiv \left(\langle v_n^6\rangle - 9\langle v_n^4\rangle\langle v_n^2\rangle + 12\langle v_n^2\rangle^3\right)/4, \\
v_n\{8\}^8 &\equiv -\left(\langle v_n^8\rangle - 16\langle v_n^6\rangle\langle v_n^2\rangle - 18\langle v_n^4\rangle^2 + 144\langle v_n^4\rangle\langle v_n^2\rangle^2 - 144\langle v_n^2\rangle^4\right)/33 \\
&\vdots
\end{aligned} \tag{6}$$

where $\langle v_n^{2k}\rangle$ denotes the cosine average of the azimuthal angle of all combinations of $m = 2k$ particles,

$$\langle v_n^{2k}\rangle = \left\langle \cos\sum_{j=1}^{k} n\left(\phi_{2j} - \phi_{2j-1}\right)\right\rangle \equiv \int v_n^{2k} p\left(v_n\right) dv_n. \tag{7}$$

The measured cumulants each have varying sensitivity to "non-flow" correlations such as resonance decays and di-jet correlations. The cumulants are constructed such that higher-orders ($k > 1$) suppress effects from non-flow as well as fluctuations [22]. In the absence of non-flow, $\langle v_n^{2k}\rangle$ is equivalent to the corresponding moment of $p\left(v_n\right)$, for all k values. If $p\left(v_n\right)$ is a Bessel-Gaussian, as shown in Eq. 4, then the cumulants have the form [23]:

$$v_n\{2k\} = \begin{cases} \sqrt{\left(v_n^{RP}\right)^2 + 2\delta^2_{\vec{v}_n}} & k = 1 \\ v_n^{RP} & k > 1 \end{cases}. \tag{8}$$

Recently, the ATLAS collaboration introduced a new experimental method to extract $p\left(v_n\right)$ directly using an unfolding technique [24], allowing for detailed studies of the behavior of flow (and ultimately geometry) fluctuations through precise extraction of the cumulants. The observation that $v_n\{4\} \approx v_n\{6\} \approx v_n\{8\}$ in PbPb collisions suggests that the flow fluctuations are Gaussian in nature [13, 25–27]. However, there is great interest in the field to observe a breakdown in the Gaussian model of fluctuations, as this is predicted by hydrodynamic models [28, 29]. A fine-structure splitting between $v_n\{4\}$ and $v_n\{6\}$ has been observed by ATLAS based on direct m-particle cumulant measurements [27].

In a recent publication [28], non-Gaussian fluctuations are found to lead to a negative skewness of $p\left(v_2\right)$ that results from the conditions that $\varepsilon_2^{RP} < 1$ and that the flow response is linear. The standardized skewness used to express this deviation from a Gaussian behavior is a dimensionless quantity and, for elliptic flow, can be expressed as

$$\gamma_1 \equiv \frac{\left\langle \left(v_2^{\mathrm{RP}} - \left\langle v_2^{\mathrm{RP}} \right\rangle\right)^3 \right\rangle}{\left(\sqrt{\left\langle \left(v_2^{\mathrm{RP}}\right)^2 \right\rangle - \left\langle v_2^{\mathrm{RP}} \right\rangle^2}\right)^3}, \tag{9}$$

where the flow harmonics are determined with respect to the "true" reaction plane, which is the angle defined by the shortest distance between the centers of the two colliding nuclei. Since the actual reaction plane is not experimentally accessible, it was proposed in reference [28] to estimate the standardized skewness of Eq. 9 in terms of the multi-particle cumulants, with

$$\gamma_1^{exp} \equiv -6\sqrt{2} v_2\left\{4\right\}^2 \frac{v_2\left\{4\right\} - v_2\left\{6\right\}}{\left(v_2\left\{2\right\}^2 - v_2\left\{4\right\}^2\right)^{3/2}}. \tag{10}$$

Precision measurements of cumulant flow harmonics and the corresponding standardized skewness are presented based on the event-by-event unfolding technique in PbPb collisions at $\sqrt{s_{NN}} = 5.02$ TeV. Distributions are determined for 5% wide centrality bins, each with an integrated η (p_{T}) range $|\eta| \leq 1.0$ ($0.3 \leq p_{\mathrm{T}} \leq 3.0$ GeV/c) where $\eta \equiv -\ln\tan\theta/2$.

2 The CMS Detector

The key feature of the Compact Muon Solenoid (CMS) detector is its 6 m internal diameter superconducting solenoid capable of producing magnetic fields up to 3.8 T. Located within the solenoid is the silicon tracker that consists of 1440 silicon pixel and 15 148 silicon strip modules. The tracker is used to measure charged particles with extreme precision in the eta range of $|\eta| \leq 2.5$. For non-isolated particles of $1 < p_{\mathrm{T}} < 10$ GeV and $|\eta| < 1.4$, the track resolutions are typically 1.5% in p_{T} and 25–90 (45–150) μm in the transverse (longitudinal) impact parameter [30]. Beyond the tracker is a lead tungstate crystal electromagnetic calorimeter (ECAL). that consists of barrel and endcap regions that provide coverage up to $|\eta| \leq 3.0$. Beyond ECAL is a brass scintillator hadron calorimeter (HCAL) that consists of barrel and endcap regions that provide the same η-coverage. CMS also has forward hadron calorimetry (HF) with quartz fibers read out by photomultipliers included to extend the coverage of the barrel and endcap calorimeters to $|\eta| \leq 5.2$. Calorimeter cells are grouped in projective towers of granularity in pseudorapidity and azimuthal angle given by $\Delta\eta \times \Delta\phi = 0.087 \times 0.087$. More information on the technical aspects of the CMS detector and its coordinate system can be found in Ref. [31].

3 Event and Track Selection

The minimum-bias trigger used in this analysis is triggered by coincident signals from both ends of the CMS detector using the HF detectors. In addition, the trigger is required to be in coincidence with the presence of both colliding bunches at the interaction point. This requirement largely suppresses events due to noise (*e.g* cosmic rays, double-firing triggers, and beam backgrounds). The minimum bias trigger is fully efficient for the centrality range 0-90%.

Events are further selected offline by requiring at least three hits in both HF calorimeters with at least 3 GeV of energy in each cluster. Events are also required to have a reconstructed primary vertex, containing at least two tracks, located within 15 cm of the nominal collision point along the beam axis. In addition, vertices are filtered on their pixel cluster compatibility. This filter removes the bottom percent of vertices with poor compatibility and suppresses contamination from pileup events.

Tracks are required to be compatible with the primary vertex, having a longitudinal association significance (d_z/σ_{d_z}) and impact parameter significance (d_0/σ_{d_0}) less than three. In addition, the relative error for the p_{T} of each track, $\sigma_{p_{\mathrm{T}}}/p_{\mathrm{T}}$, is required to be less than 10% and tracks are required to have at least 11 hits along their trajectory in the pixel and strip trackers. To reduce the number of misidentified tracks, the χ^2 of the track's fit divided by the total number of degrees of freedom and the total number of layers with hits along the track's trajectory must be less that 0.15.

Tracking performance is evaluated in terms of tracking efficiency, fake reconstruction rates, and multiple reconstruction rates in different centrality, p_{T}, and η ranges. To determine the tracking performance, a large sample of PYTHIA + HYDJET [32, 33] events were generated and propagated through a GEANT4 simulation [34]. Primary track reconstruction has a combined geometric acceptance and efficiency exceeding 60% for $p_{\mathrm{T}} \approx 1.0$ GeV/c and $|\eta| < 1.0$. When track p_{T} is below 1 GeV/c, the acceptance and efficiency steadily drops, reaching approximately 40% at $p_{\mathrm{T}} \approx 0.3$ GeV/c. The efficiency is not strongly dependent on centrality and the rate of misidentified tracks is smaller than 8% for the most central events.

4 Analysis Technique

4.1 Event-by-Event Flow Observables

In any given collision, the number of particles emitted is finite and the v_n coefficients can only be estimated. These estimates are made by:

$$\begin{aligned} v_{n,x}^{raw} &= |\vec{v}_n^{raw}| \cos n\Psi_n^{raw} = \langle \cos n\phi \rangle, \\ v_{n,y}^{raw} &= |\vec{v}_n^{raw}| \sin n\Psi_n^{raw} = \langle \sin n\phi \rangle, \\ |\vec{v}_n^{raw}| &= \sqrt{\left(v_{n,x}^{raw}\right)^2 + \left(v_{n,y}^{raw}\right)^2}, \end{aligned} \tag{11}$$

where $\langle \dots \rangle$ denotes an average over all particles in a given range of phase space. In the limit of large particle multiplicities, and in absence of non-flow, the event-estimated flow values approach the true flow values for each event. Events are split into different centrality classes and the estimated flow values are used to construct "observed" event-by-event $p\left(v_n^{obs}\right)$ distributions in each class.

Potential biases from non-uniform detector acceptance must be properly accounted for when calculating event-by-event observed flow vectors. To recover first-order effects that arise with non-uniform detector acceptances, tracks are weighted by their tracking efficiencies. In doing so, Eq. 11 becomes:

$$\begin{aligned} v_{n,x}^{raw} &= \frac{\sum_i w_i \cos n\phi}{\sum_i w_i}, \\ v_{n,y}^{raw} &= \frac{\sum_i w_i \sin n\phi}{\sum_i w_i} \end{aligned} \tag{12}$$

where $w_i = 1/\varepsilon\left(p_{\mathrm{T}}, \eta\right)$ are the inverse tracking efficiencies for each track. In addition to track reweighting, a standard recentering procedure [35] is applied to each event class to further suppress non-uniform detector acceptance biases. In the recentering technique, an average flow vector $\vec{v}_n^{det}$ is calculated over all events in a given centrality class and then subtracted from the raw flow vectors (Eq. 12) on an event-by-event basis:

$$\begin{aligned} \vec{v}_n^{det} &= \frac{\sum_{Events} \vec{v}_n^{raw}}{N_{Events}}, \\ \vec{v}_n^{obs} &= \vec{v}_n^{raw} - \vec{v}_n^{det}. \end{aligned} \tag{13}$$

Finite particle multiplicities result in a statistical smearing of $\vec{v}_n^{obs}$ about the true underlying $\vec{v}_n$ on an event-by-event basis. This, in turn, results in a $p\left(\vec{v}_n^{obs}\right)$ that is statistically smeared about a true underlying $p\left(\vec{v}_n\right)$. It is of interest to remove the smearing effects from the observed distributions to allow for detailed studies of event-by-event fluctuations in the v_n coefficients. This analysis uses unfolding to remove the smearing effects from $p\left(v_n^{obs}\right)$ and obtain $p\left(v_n\right)$ directly. Details of this unfolding technique are discussed in Sec. 4.3.

4.2 The Response Function

The event-by-event observed flow vectors are statistically smeared about the true underlying event flow vectors by a 2D response function $p\left(\vec{v}_n^{obs}|\vec{v}_n\right)$. The response function is a conditional probability measuring the probability that, for a given event, one observes a flow vector $\vec{v}_n^{obs}$ when the underlying flow vector is $\vec{v}_n$. The distribution of event-by-event observed flow vectors can be expressed as a convolution of the true underlying distribution of flow vectors and the response function:

$$p\left(\vec{v}_n^{obs}\right) = p\left(\vec{v}_n^{obs}|\vec{v}_n\right) \times p\left(\vec{v}_n\right). \tag{14}$$

In heavy-ion experiments it is typical to work with flow vector magnitudes and binned data and the convolution can be rewritten as:

$$p\left(v_{n,i}^{obs}|v_{n,j}\right) \times p\left(v_{n,j}\right) = p\left(v_{n,i}^{obs}\right), \tag{15}$$

where $p\left(v_{n,i}^{obs}|v_{n,j}\right)$ corresponds to the response matrix. The response matrix can be used to remove the smearing effects from $p\left(v_{n,i}^{obs}\right)$ using D'Agostini iteration unfolding [36–38].

A critical step in this analysis is determining the correct response matrix to unfold the smearing effects from the observed $p\left(v_n^{obs}\right)$ distribution. A data-driven technique to build the response matrix was introduced by the ATLAS collaboration in Ref. [24] which is utilized in this analysis. This technique works for symmetric collisions such as the PbPb collisions studied at the LHC.

For a given class of events, tracks are split into two symmetric subevents. Tracks are measured by the silicon tracker and subevents are chosen based on track η. All tracks with $\eta > 0$ fall in subevent a while all tracks with $\eta < 0$ fall in subevent b. For each subevent, flow vectors are calculated using Eqs. 12 and 13 and $p\left(\vec{v}_n^{obs}\right)$ distributions are built. On average, $v_n\left(\eta\right)$ is symmetric about $\eta = 0$, and the physical flow signal cancels in the distribution of the flow vector difference between the two subevents $p\left(\vec{v}_n^{obs,a} - \vec{v}_n^{obs,b}\right)$. Therefore, the resulting subevent difference distribution contains only the effects from statistical smearing and non-flow [39].

With the assumption that the subevent difference distribution is an accurate description of the smearing effects present in data, it can then be used to build the response matrix. For centrality intervals up to 50%, the subevent difference distribution is described well by a 2D Gaussian centered at zero and for more peripheral events, it is better described by a 2D non-standardized Student's t-distribution centered at zero. This fit performance is illustrated in Fig. 1. The Gaussian nature coupled to a mean of zero in the subevent difference distributions suggests that the smearing is statistical in nature.

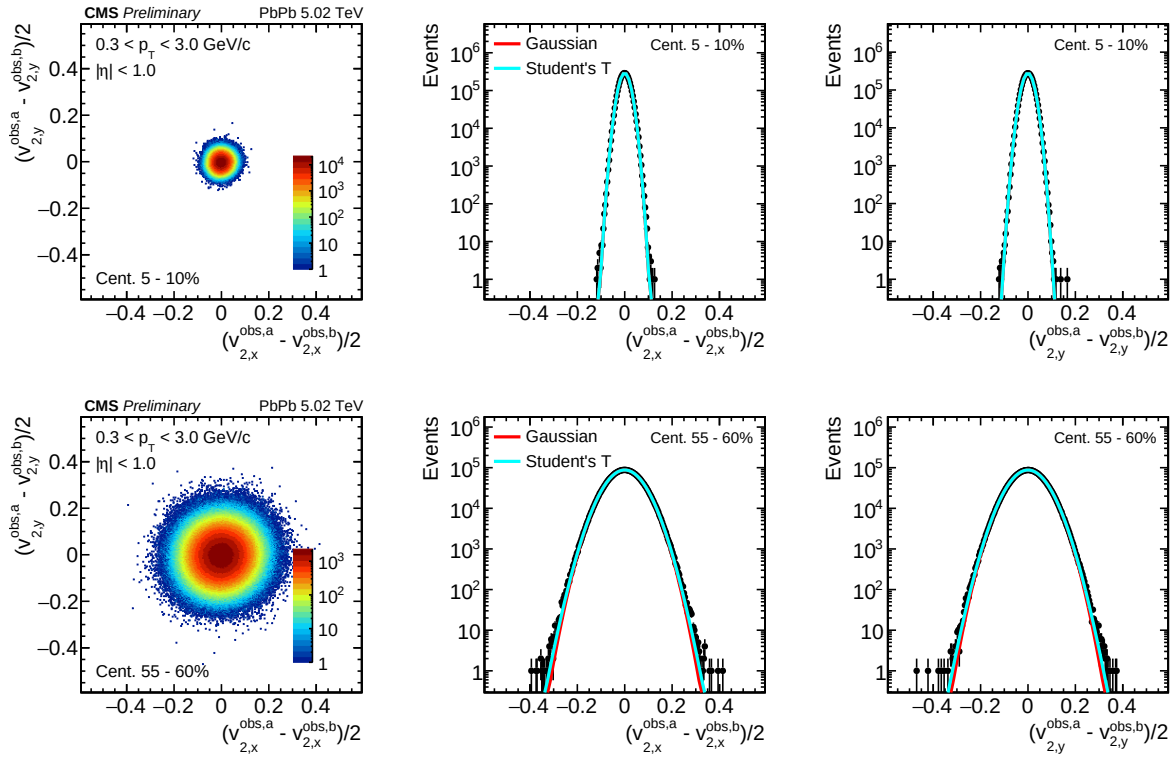

Figure 1: Fit performance of a Gaussian and Student's t-distribution to the rescaled subevent difference distributions for events in the 5–10% (top row) and 55–60% centrality classes (bottom row). Central events have a large number of tracks in each subevent, thus the Gaussian and Student's t-functions both describe the data well. The difference in fit performance is more pronounced in peripheral events where the small number of tracks per event is in the regime where the Student's t-function is relevant.

Before the subevent difference distribution can be used to build the response function, it must first be rescaled to properly account for the sample sizes used. Because there are half as many tracks in each subevent compared to the full event, the smearing effects are different. For Gaussian random variables, the standard deviation of a population is inversely proportional to the square root of the sample size. In addition, the variance of a distribution obtained from the difference between two Gaussian random variables can be expressed as $\sigma^2_{a-b} = \sigma^2_a + \sigma^2_b$. Since, on average, the number of tracks in each subevent is half that of the full event and the variances of the subevent difference distributions are equal, the smearing width obtained from the subevent difference distribution will be a factor of two larger than that of the full event. The mean is not affected from the sample size difference. Therefore, scaling the subevent difference distribution down by a factor of two $p\left(\vec{v}_n^{obs,a} - \vec{v}_n^{obs,b}\right) \rightarrow p\left(\left[\vec{v}_n^{obs,a} - \vec{v}_n^{obs,b}\right]/2\right)$ will provide the correct description of the smearing present in the full event.

A purely data-driven response function can be built from the rescaled subevent difference distribution. As previously mentioned, the rescaled subevent difference distribution is a measure of the smearing effects for the full event and can be rewritten as

$$p\left(\left[\vec{v}_n^{obs,a} - \vec{v}_n^{obs,b}\right]/2\right) = p\left(\vec{s}\right) = p\left(\vec{v}_n^{obs} - \vec{v}_n\right). \tag{16}$$

Therefore, with an assumed form of the true underlying event-by-event flow distribution (prior), the response matrix can be built on an event-by-event basis. This is achieved by throwing a random flow vector based on the prior and throwing a random smearing vector from Eq. 16. Adding these two vectors together provides an estimator of $\vec{v}_n^{obs}$ for the event. This procedure can be repeated up to the number of events used to build the subevent difference distribution. By keeping the magnitudes of the vectors, each iteration will provide one entry of v_n^{obs} and v_n to the response matrix in Eq. 15.

4.3 Unfolding

The default method for unfolding in this analysis is D'Agostini iteration with early stopping, as outlined in Refs. [36–38]. The RooUnfold [40] package for the ROOT data analysis framework [41] contains software for this unfolding technique and is utilized in this analysis. The goal of this technique is to determine a maximum-likelihood estimate (MLE) of the true underlying event-by-event flow distribution. The unfolding workflow can be summarized by:

$$\hat{p}\left(v_{n,i}\right)^{iter+1} = \sum_j \hat{M}_{ij}^{iter} p\left(v_{n,j}^{obs}\right) \tag{17}$$

where $\hat{p}\left(v_{n,i}\right)^{iter+1}$ is a vector that represents an estimator for the true underlying distribution, $p\left(v_{n,j}^{obs}\right)$ is a vector that represents the observed distribution, and $\hat{M}_{ij}^{iter}$ is the unfolding matrix. In this case, binned data are represented by vectors and matrices. The unfolding matrix is constructed using the prior and response matrix determined in Sec. 4.2. The unfolding matrix has the form

$$\hat{M}_{ij}^{iter} = \frac{p\left(v_{n,j}^{obs}|v_{n,i}\right)\hat{p}\left(v_{n,i}\right)^{iter}}{\left[\sum_l p\left(v_{n,j}^{obs}|v_{n,l}\right)\hat{p}\left(v_{n,l}\right)^{iter}\right]\left[\sum_m p\left(v_{n,m}^{obs}|v_{n,i}\right)\right]} \tag{18}$$

where $\hat{p}\left(v_{n,i}\right)^0$ corresponds to the prior and $p\left(v_{n,j}^{obs}|v_{n,i}\right)$ is the response matrix. Each iteration will then produce an estimator of the true distribution. If the prior is close to the true distribution, the procedure will converge after a few iterations. If run until convergence, the procedure will output a MLE of the true underlying distribution. The correct choice in prior is not necessary for this response matrix to be successful. In cases of complete physical ignorance it is recommended to use a uniform distribution and then update when more information is available. In this analysis, an acceptable prior is the distribution of observed flow vectors. For example, in event classes with large particle multiplicities, the smearing effects are small and the observed flow vector distribution is very similar to the true underlying distribution.

Given the mathematically ill-posed nature of the unfolding procedure, when the number of iterations is allowed to run to large values, the result becomes increasingly sensitive to statistical fluctuations. This will give rise to unphysical oscillations in the unfolded distribution. These features can be suppressed by stopping iterations at some predefined point and by choosing a

prior that is close to the true distribution. The iteration cutoff is entirely problem dependent and a clear criterion for the cutoff point must be defined.

The criteria for iteration cutoff in this analysis is defined by applying the response matrix to each unfolding iteration ("refolding") and comparing to the observed distribution. The motivation for this is shown in Eq. 15 by replacing $p\left(v_{n,j}\right)$ with a distribution obtained from unfolding. If the unfolding procedure has converged on the MLE of $p\left(v_{n,j}\right)$, then refolding will reproduce $p\left(v_{n,i}^{obs}\right)$. Therefore, iterations are stopped when the χ^2/NDF goodness of fit between the refolded and observed distributions is near 1.0. After a final unfolding iteration is selected the resulting distribution is truncated above $\langle v_n \rangle + 4\sigma_{v_n}$ to suppress residual biases in the tail from the unfolding procedure.

4.4 Extracting Eccentricity Distributions from Flow Distributions

Elliptic flow is a direct reflection of the medium's response to the initial collision geometry [10] and provides insight into its fundamental transport properties [42–44]. In several studies [14, 44–46] the proportionality between eccentricity and flow harmonics is assumed to be linear. In this analysis, the unfolded $p\left(v_2\right)$ distributions are used to infer the nature of $p\left(\varepsilon_2\right)$ distributions. To achieve this aim, $p\left(\varepsilon_2\right)$ distributions are assumed to have a universal elliptic power law parametrization [46]:

$$p(\varepsilon_2) = \frac{2\alpha\varepsilon_2}{\pi}(1-\varepsilon_0^2)^{\alpha+1/2}\int_0^{\pi}\frac{(1-\varepsilon_2^2)^{\alpha-1}d\varphi}{(1-\varepsilon_0\varepsilon_2\cos\varphi)^{2\alpha+1}}, \tag{19}$$

where ε_0 is approximately equal to the mean eccentricity in the reaction plane (strict equality is expected in PbPb collisions) and α describes the eccentricity fluctuations. This parametrization was shown to describe the eccentricity distributions in pp, pPb, and PbPb collisions well using the MC-Glauber and MC-KLN initial-state models [14]. In cases where $\alpha \gg 1$ and $\varepsilon_0 \ll 1$ the universal elliptic power law distribution reduces to Bessel-Gaussian. By assuming a linear response between eccentricity and flow, $v_2 = k_2\,\varepsilon_2$, eccentricity distributions can be inferred from flow distributions without any assumption on an initial-state model:

$$p\left(v_2\right) = \tfrac{d\varepsilon_2}{dv_2}\,p\left(\varepsilon_2\right) \tag{20}$$

$$p\left(\frac{v_2}{k_2}\right) = k_2\,p\left(v_2\right) \tag{21}$$

In contrast to the scale invariant Bessel-Gaussian, k_2 factorizes when fluctuations are non-Gaussian. Therefore, an elliptic power law fit to $p(v_2)$ is able to return all three parameters: k_2, ε_0, and α.

4.5 Systematic Uncertainties

Systematic uncertainties are determined for two cases in this analysis. The first case deals with the systematic uncertainty on the scale of v_2, where studies are performed to assess the bias on the quantities extracted from $p(v_2)$, such as the cumulant flow harmonics. There are five primary contributions to the systematic bias on the scale of v_2: 1) vertex position cut, 2) response matrix uncertainty, 3) pileup contamination, 4) unfolding regularization, and 5) track quality cuts. The most stable observables in all tests are the higher-order cumulant ratios while the least stable observable is the skewness.

The scale systematic uncertainties that arise from the cut on the vertex z-position are investigated by splitting the default vertex cut into two scenarios. In the first scenario, the vertex position window is restricted to $|v_z| \leq 3.0$ cm, while the second window will contain the remainder

of possible vertex positions, $3.0 \leq |v_z| \leq 15.0$ cm. The maximum variation between the two scenarios relative to the default window is recorded as a systematic uncertainty. The vertex cut systematic uncertainty is the most dominant, having a $\approx 1\%$ effect on the higher-order cumulant ratios. To estimate the systematic uncertainty on the choice of response matrix, unfolding is repeated using an analytic Gaussian response matrix built from the subevent difference distributions. The full variations between the two approaches are used as a systematic uncertainty. The response matrix systematic uncertainty is the second-most dominant, having a $\approx 0.5\%$ effect on the higher-order cumulant ratios. To assess the potential bias from pileup events, the vertex-cluster compatibility event selection is strengthened to further filter out potential pileup events. Variations in observables from the two pileup scenarios are recorded as a systematic uncertainty. The pileup systematic uncertainty is less dominant, having a $\approx 0.1\%$ effect on the higher-order cumulant ratios. The scale bias from unfolding regularization is studied in detail by modifying the χ^2/NDF goodness-of-fit criteria between the observed and refolded distributions. If the χ^2/NDF criteria is too loose, then the analysis will select unfolding distributions using fewer iterations. The loose scenario tends to bias unfolding distributions toward the prior. On the other hand, if the χ^2/NDF criteria is too tight, then more iterations will be required for the procedure to converge. The tight scenario runs the risk of unphysical oscillations arising in the unfolded distributions. An estimation of the regularization bias determined from the maximum variation in observables when the refold χ^2/NDF cutoff is 2.0 relative to when it is 1.0. The track quality systematic uncertainty is less dominant, having a $\approx 0.1\%$ effect on the higher-order cumulant ratios. To estimate the effect that misidentified tracks have on event-by-event unfolded distributions, track quality cuts are split into "loose" and "tight" scenarios. The maximum variation between the two scenarios relative to the default track selection is recorded as a systematic uncertainty. The track quality systematic uncertainty is negligible, having a $< 0.1\%$ effect on the higher-order cumulant ratios.

An additional conservative systematic uncertainty of 7% was placed on γ_1^{exp} as it was the only observable found to be sensitive to the p_{T} resolution of the tracker. Total systematic uncertainties are determined by adding the contribution from each study in quadrature.

The second case deals with the systematic uncertainty on the shape of $p(v_2)$, namely the bin-to-bin uncertainties in the selected unfolded distributions. There are six studies performed to assess the shape bias: the same five from the scale studies and an additional study on the response matrix element uncertainties.

Shape systematic uncertainties from the finite number of events used to make the response functions used for unfolding are determined by propagating the uncertainties on the unfolding matrix elements through the unfolding procedure as outlined in Ref. [40]. In addition, unfolded distributions from the remaining five systematic studies are rescaled to have the same mean as the default unfolded distributions. Bin-to-bin variations relative to the default case are taken as systematic uncertainties. To suppress effects from statistical fluctuations, bin-to-bin variations are first smoothed to the general trend. The final systematic shape uncertainties are obtained by adding the contributions from each study in quadrature. The shape uncertainties can be seen in Fig. 6 where the unfolded distributions are presented.

5 Results

Primary results for this analysis are obtained by performing event-by-event unfolding on events in 5% wide centrality bins up to 60% using the standard track selection described in Sec. 3. Figure 2 shows the cumulant values extracted from the unfolded $p\,(v_2)$ distributions. The cumulants show the expected behavior of $v_2\{2\} > v_2\{4\} \approx v_2\{6\} \approx v_2\{8\}$, however a splitting between the higher order cumulants can already be seen in the peripheral bins. We further quantify this splitting by looking at the ratio of higher-order cumulants in Fig. 3. As stated earlier, the observation that $v_2\,\{4\} \approx v_2\,\{6\} \approx v_2\,\{8\}$ is consistent with the Gaussian fluctuation model for flow harmonics. A statistically significant fine structure splitting between $v_2\,\{4\}$, $v_2\,\{6\}$, and $v_2\,\{8\}$ is observed on the percent level for most centrality bins. The results of Fig. 3 are further supported by Fig. 4 where the first measurement of the estimate skewness with respect to the reaction plane (γ_1^{exp}) is presented. If the model of flow harmonic fluctuations is Gaussian, then the skewness of $p\,(v_2)$ would be consistent with zero. The estimate skewness parameter is non-zero for the same centrality bins that present a significant fine structure splitting in the higher-order cumulants. Theoretical predictions from Ref. [28] are available to compare to the measured $v_2\{6\}/v_2\{4\}$ and γ_1^{exp} and are shown in the respective figures as colored bands. It should be noted that these predictions were made for $\sqrt{s_{NN}} = 2.76$ TeV, but the measured quantities are not expected to change dramatically between 2.76 and 5.02 TeV.

Cumulant ratios are also compared to those measured by the ATLAS collaboration at $\sqrt{s_{NN}} = 2.76$ TeV [27] in Fig. 5. It should be noted that the track selection for ATLAS differs from CMS in this comparison. CMS selects tracks with $0.3 < p_{\mathrm{T}} < 3.0$ GeV and $|\eta| < 1.0$, whereas ATLAS selects tracks with $0.5 < p_{\mathrm{T}} < 20.0$ GeV and $|\eta| < 2.5$. The results from CMS and ATLAS are consistent within uncertainties.

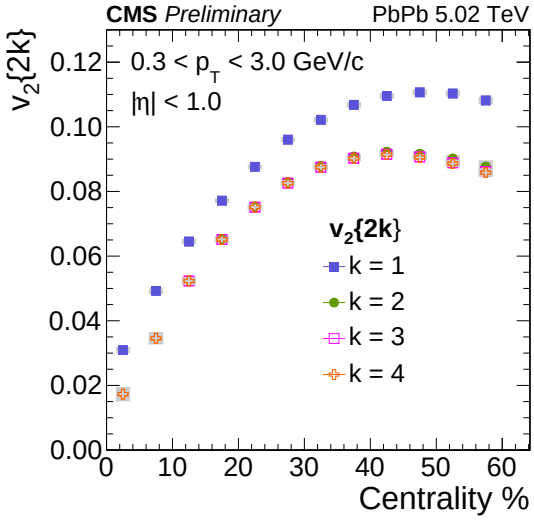

Figure 2: Cumulant values extracted from the unfolded $p\,(v_2)$ distributions exhibiting the expected $v_2\{2\} > v_2\{4\} \approx v_2\{6\} \approx v_2\{8\}$ behavior. Both statistical and systematic uncertainties are shown. A fine-level splitting of the higher-order cumulants becomes more pronounced in peripheral bins.

In addition, unfolded $p(v_2)$ distributions were fitted using the transformed elliptic power law parametrization (Eq. 20) and the Bessel-Gaussian parametrization (Eq. 5) to gain further insight as to the nature of the initial-state fluctuations. Fig. 6 demonstrates the $p(v_2)$ fit performance for 5% centrality classes for both the elliptic power and Bessel-Gaussian parametrizations. Fit qual-

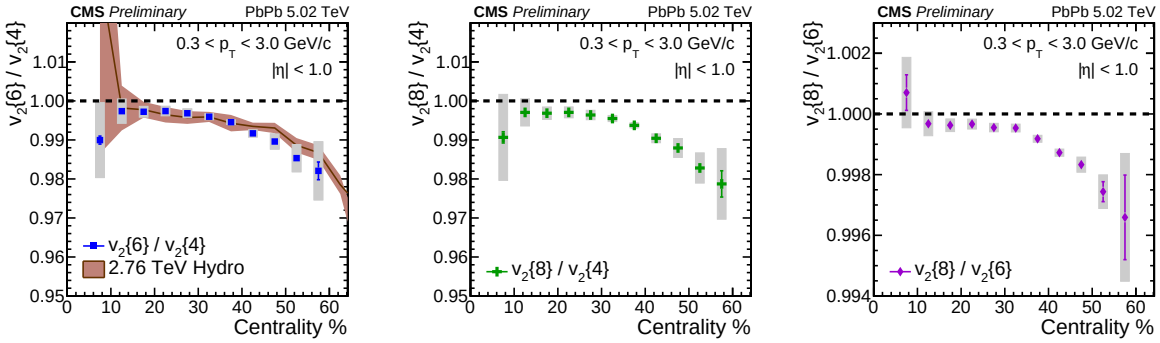

Figure 3: Ratios of higher-order cumulants with values obtained from the moments of the unfolded $p\,(v_2)$ distributions. Both statistical and systematic uncertainties are shown. Hydrodynamic predictions for 2.76 TeV from Ref. [28] are presented as a colored band and are compared to the measured ratio $v_2\{6\}/v_2\{4\}$. Theory predictions are consistent to the measurement within uncertainties.

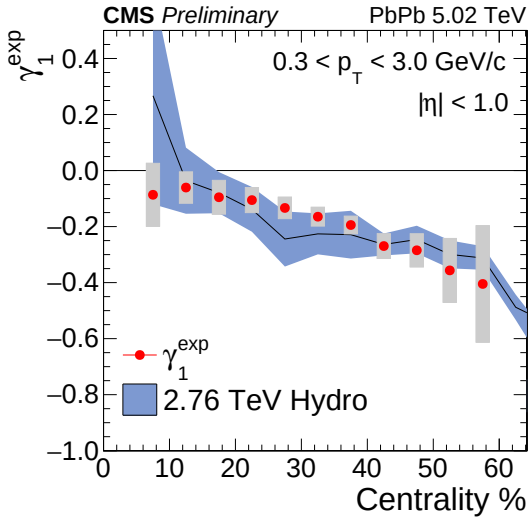

Figure 4: The estimated skewness for the unfolded $p\,(v_2)$ as determined from its cumulant flow harmonics with Eq. 10. Both statistical and systematic uncertainties are shown. Hydrodynamic predictions for 2.76 TeV from Ref. [28] are presented as a colored band and are compared to the measured skewness. Theory predictions are consistent to the measurement within uncertainties.

ities are assessed by refolding the fits using the response function and determining a χ^2/NDF goodness-of-fit with respect to the observed distribution. In all cases the elliptic power law parametrization better describes the fluctuations, yielding a χ^2/NDF goodness-of-fit closer to one than for the Bessel-Gaussian.

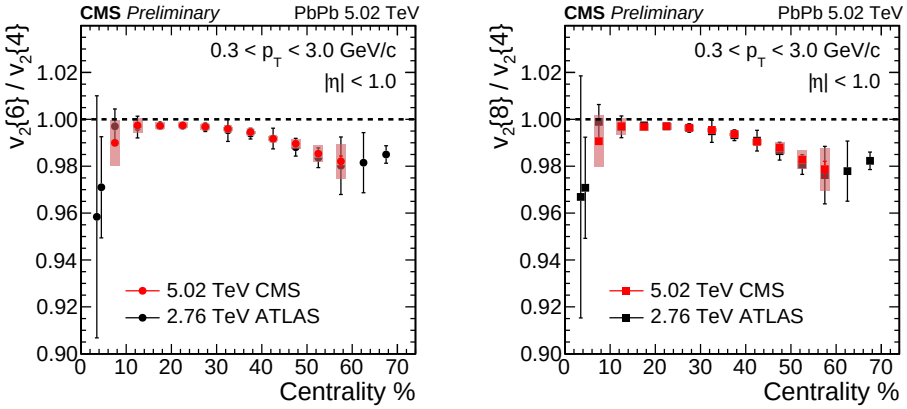

Figure 5: Ratios of higher-order cumulants with values obtained from the moments of the unfolded $p\,(v_2)$ distributions measured by CMS compared to those measured by ATLAS in Ref. [27]. Both statistical and systematic uncertainties are shown for CMS as error bars and bands respectively. ATLAS uncertainties are presented as statistical and systematic added in quadrature.

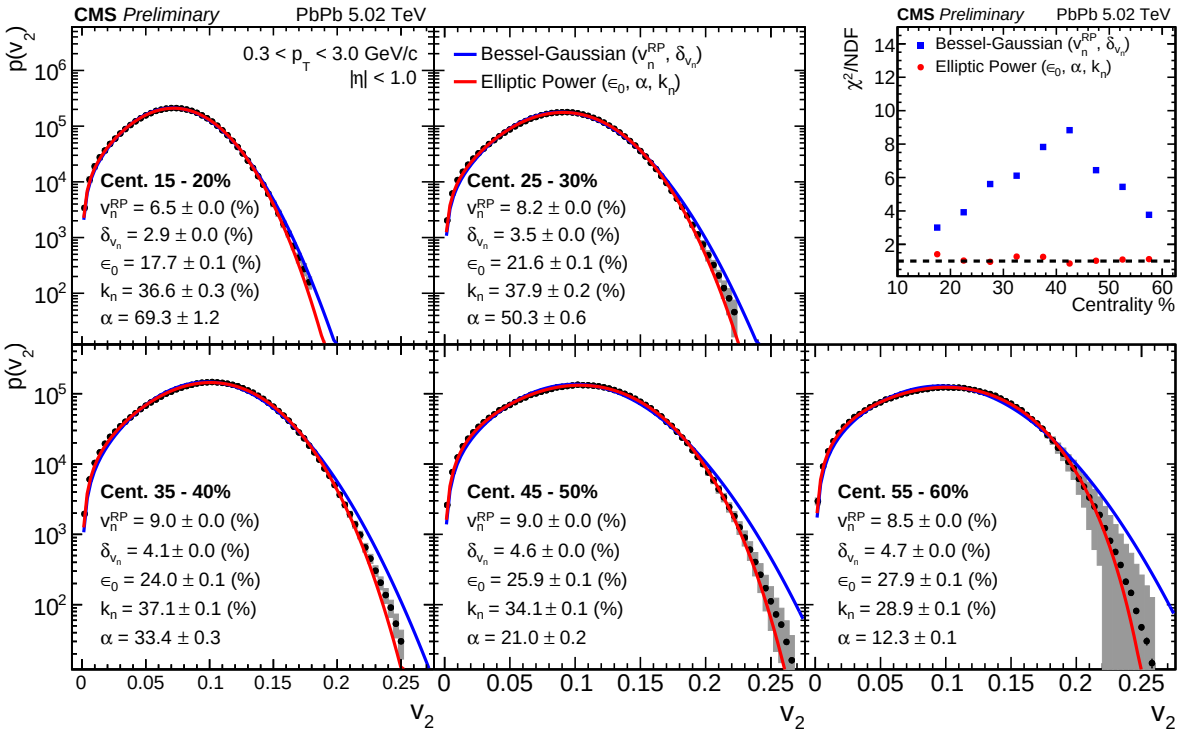

Figure 6: Elliptic power law (Eq. 19) and Bessel-Gaussian (Eq. 5) parametrizations fitted to unfolded $p(v_2)$ distributions. Parameters extracted from each fit are provided in each panel with respective statistical uncertainties. All parameters except α are reported as percentages. Fit performance, as measured by the smeared-space χ^2/NDF goodness-of-fit, is presented as a function of centrality for each parametrization.

6 Summary

In summary, non-Gaussian behavior in the fluctuations of v_2 coefficients has been observed in PbPb collisions at $\sqrt{s_{NN}} = 5.02\,\text{TeV}$. This observation was made by unfolding the statistical smearing effects in observed flow harmonic distributions to obtain the underlying event-by-event flow distributions for 5% wide centrality bins up to 60%. Cumulant flow harmonics were calculated from the moments of the underlying distributions and a fine-structure splitting was observed between $v_2\{4\}$, $v_2\{6\}$, and $v_2\{8\}$. In addition, the standardized skewness with respect to the reaction plane was estimated using the cumulants and was found to have a non-zero value, whose magnitude increases with centrality. Both measurements are consistent with a breakdown in the Gaussian model of elliptic flow fluctuations.

In addition, Bessel-Gaussian and elliptic power law parametrizations were fitted to the unfolded $p(v_2)$ distributions to gain further insight as to the nature of the initial-state fluctuations. Both parametrizations assume a linear response between eccentricity and flow, but only the elliptic power law contains the physical constraint $\varepsilon_2 < 1$. This constraint naturally incorporates skewness and allows the elliptic power law parametrization to provide a more accurate description of $p(v_2)$ (and ultimately $p(\varepsilon_2)$) than the Bessel-Gaussian parametrization.

References

[1] BRAHMS Collaboration, "Quark gluon plasma and color glass condensate at RHIC? The Perspective from the BRAHMS experiment", *Nucl. Phys.* **A757** (2005) 1–27, doi:10.1016/j.nuclphysa.2005.02.130, arXiv:nucl-ex/0410020.

[2] PHENIX Collaboration, "Formation of dense partonic matter in relativistic nucleus-nucleus collisions at RHIC: Experimental evaluation by the PHENIX collaboration", *Nucl. Phys.* **A757** (2005) 184–283, doi:10.1016/j.nuclphysa.2005.03.086, arXiv:nucl-ex/0410003.

[3] B. B. Back et al., "The PHOBOS perspective on discoveries at RHIC", *Nucl. Phys.* **A757** (2005) 28–101, doi:10.1016/j.nuclphysa.2005.03.084, arXiv:nucl-ex/0410022.

[4] STAR Collaboration, "Experimental and theoretical challenges in the search for the quark gluon plasma: The STAR Collaboration's critical assessment of the evidence from RHIC collisions", *Nucl. Phys.* **A757** (2005) 102–183, doi:10.1016/j.nuclphysa.2005.03.085, arXiv:nucl-ex/0501009.

[5] ATLAS Collaboration, "Observation of a Centrality-Dependent Dijet Asymmetry in Lead-Lead Collisions at $\sqrt{s_{NN}} = 2.77$ TeV with the ATLAS Detector at the LHC", *Phys. Rev. Lett.* **105** (2010) 252303, doi:10.1103/PhysRevLett.105.252303, arXiv:1011.6182.

[6] CMS Collaboration, "Observation and studies of jet quenching in PbPb collisions at nucleon-nucleon center-of-mass energy = 2.76 TeV", *Phys. Rev.* **C84** (2011) 024906, doi:10.1103/PhysRevC.84.024906, arXiv:1102.1957.

[7] H. Song, "QGP viscosity at RHIC and the LHC - a 2012 status report", *Nucl. Phys.* **A904-905** (2013) 114c–121c, doi:10.1016/j.nuclphysa.2013.01.052, arXiv:1210.5778.

[8] U. Heinz, C. Shen, and H. Song, "The viscosity of quark-gluon plasma at RHIC and the LHC", *AIP Conf. Proc.* **1441** (2012) 766–770, doi:10.1063/1.3700674, arXiv:1108.5323.

[9] J.-Y. Ollitrault, "Anisotropy as a signature of transverse collective flow", *Phys. Rev.* **D46** (1992) 229–245, doi:10.1103/PhysRevD.46.229.

[10] B. Alver and G. Roland, "Collision geometry fluctuations and triangular flow in heavy-ion collisions", *Phys. Rev.* **C81** (2010) 054905, doi:10.1103/PhysRevC.82.039903, 10.1103/PhysRevC.81.054905, arXiv:1003.0194. [Erratum: Phys. Rev.C82,039903(2010)].

[11] M. L. Miller, K. Reygers, S. J. Sanders, and P. Steinberg, "Glauber modeling in high energy nuclear collisions", *Ann. Rev. Nucl. Part. Sci.* **57** (2007) 205–243, doi:10.1146/annurev.nucl.57.090506.123020, arXiv:nucl-ex/0701025.

[12] D. Teaney and L. Yan, "Triangularity and Dipole Asymmetry in Heavy Ion Collisions", *Phys. Rev.* **C83** (2011) 064904, doi:10.1103/PhysRevC.83.064904, arXiv:1010.1876.

[13] S. A. Voloshin, A. M. Poskanzer, A. Tang, and G. Wang, "Elliptic flow in the Gaussian model of eccentricity fluctuations", *Phys. Lett.* **B659** (2008) 537–541, doi:10.1016/j.physletb.2007.11.043, arXiv:0708.0800.

[14] L. Yan and J.-Y. Ollitrault, "Universal fluctuation-driven eccentricities in proton-proton, proton-nucleus and nucleus-nucleus collisions", *Phys. Rev. Lett.* **112** (2014) 082301, doi:10.1103/PhysRevLett.112.082301, arXiv:1312.6555.

[15] Z. Qiu and U. W. Heinz, "Event-by-event shape and flow fluctuations of relativistic heavy-ion collision fireballs", *Phys. Rev.* **C84** (2011) 024911, doi:10.1103/PhysRevC.84.024911, arXiv:1104.0650.

[16] S. A. Voloshin, A. M. Poskanzer, and R. Snellings, "Collective phenomena in non-central nuclear collisions", arXiv:0809.2949.

[17] D. A. Teaney, "Viscous Hydrodynamics and the Quark Gluon Plasma", arXiv:0905.2433.

[18] S. Voloshin and Y. Zhang, "Flow study in relativistic nuclear collisions by Fourier expansion of Azimuthal particle distributions", *Z. Phys.* **C70** (1996) 665–672, doi:10.1007/s002880050141, arXiv:hep-ph/9407282.

[19] N. Borghini, P. M. Dinh, and J.-Y. Ollitrault, "A New method for measuring azimuthal distributions in nucleus-nucleus collisions", *Phys. Rev.* **C63** (2001) 054906, doi:10.1103/PhysRevC.63.054906, arXiv:nucl-th/0007063.

[20] N. Borghini, P. M. Dinh, and J.-Y. Ollitrault, "Flow analysis from multiparticle azimuthal correlations", *Phys. Rev.* **C64** (2001) 054901, doi:10.1103/PhysRevC.64.054901, arXiv:nucl-th/0105040.

[21] N. Borghini, P. M. Dinh, and J.-Y. Ollitrault, "Flow analysis from cumulants: A Practical guide", in *International Workshop on the Physics of the Quark Gluon Plasma Palaiseau, France, September 4-7, 2001*. 2001. arXiv:nucl-ex/0110016.

[22] J. Jia, "Event-shape fluctuations and flow correlations in ultra-relativistic heavy-ion collisions", *J. Phys.* **G41** (2014), no. 12, 124003, doi:10.1088/0954-3899/41/12/124003, arXiv:1407.6057.

[23] R. S. Bhalerao, M. Luzum, and J.-Y. Ollitrault, "Determining initial-state fluctuations from flow measurements in heavy-ion collisions", *Phys. Rev.* **C84** (2011) 034910, doi:10.1103/PhysRevC.84.034910, arXiv:1104.4740.

[24] ATLAS Collaboration, "Measurement of the distributions of event-by-event flow harmonics in lead-lead collisions at = 2.76 TeV with the ATLAS detector at the LHC", *JHEP* **11** (2013) 183, doi:10.1007/JHEP11(2013)183, arXiv:1305.2942.

[25] CMS Collaboration Collaboration, "Azimuthal anisotropy of charged particles from multiparticle correlations in pPb and PbPb collisions with CMS", Technical Report CMS-CR-2014-160, CERN, Geneva, Jul, 2014.

[26] ALICE Collaboration, "Multiparticle azimuthal correlations in p -Pb and Pb-Pb collisions at the CERN Large Hadron Collider", *Phys. Rev.* **C90** (2014), no. 5, 054901, doi:10.1103/PhysRevC.90.054901, arXiv:1406.2474.

[27] ATLAS Collaboration, "Measurement of flow harmonics with multi-particle cumulants in Pb+Pb collisions at $\sqrt{s_{\mathrm{NN}}} = 2.76$ TeV with the ATLAS detector", *Eur. Phys. J.* **C74** (2014), no. 11, 3157, doi:10.1140/epjc/s10052-014-3157-z, arXiv:1408.4342.

[28] G. Giacalone, L. Yan, J. Noronha-Hostler, and J.-Y. Ollitrault, "The skewness of elliptic flow fluctuations", arXiv:1608.01823.

[29] H. Gronqvist, J.-P. Blaizot, and J.-Y. Ollitrault, "Non-Gaussian eccentricity fluctuations", arXiv:1604.07230.

[30] CMS Collaboration, "Description and performance of track and primary-vertex reconstruction with the CMS tracker", *JINST* **9** (2014) P10009, doi:10.1088/1748-0221/9/10/P10009, arXiv:1405.6569.

[31] CMS Collaboration, "The CMS experiment at the CERN LHC", *JINST* **3** (2008) S08004, doi:10.1088/1748-0221/3/08/S08004.

[32] T. Sjöstrand, S. Mrenna, and P. Skands, "PYTHIA 6.4 physics and manual", *JHEP* **05** (2006) 026, doi:10.1088/1126-6708/2006/05/026, arXiv:hep-ph/0603175.

[33] I. P. Lokhtin and A. M. Snigirev, "A Model of jet quenching in ultrarelativistic heavy ion collisions and high-p(T) hadron spectra at RHIC", *Eur. Phys. J.* **C45** (2006) 211–217, doi:10.1140/epjc/s2005-02426-3, arXiv:hep-ph/0506189.

[34] GEANT4 Collaboration, "GEANT4: A Simulation toolkit", *Nucl. Instrum. Meth.* **A506** (2003) 250–303, doi:10.1016/S0168-9002(03)01368-8.

[35] A. M. Poskanzer and S. A. Voloshin, "Methods for analyzing anisotropic flow in relativistic nuclear collisions", *Phys. Rev.* **C58** (1998) 1671–1678, doi:10.1103/PhysRevC.58.1671, arXiv:nucl-ex/9805001.

[36] G. D'Agostini, "A Multidimensional unfolding method based on Bayes' theorem", *Nucl.Instrum.Meth.* **A362** (1995) 487–498, doi:10.1016/0168-9002(95)00274-X.

[37] W. H. Richardson, "Bayesian-based iterative method of image restoration", *JOSA* **62** (1972), no. 1, 55–59.

[38] L. B. Lucy, "An iterative technique for the rectification of observed distributions", *The astronomical journal* **79** (1974) 745.

[39] J. Jia and S. Mohapatra, "Disentangling flow and nonflow correlations via Bayesian unfolding of the event-by-event distributions of harmonic coefficients in ultrarelativistic heavy-ion collisions", *Phys. Rev.* **C88** (2013), no. 1, 014907, doi:10.1103/PhysRevC.88.014907, arXiv:1304.1471.

[40] T. Adye, "Unfolding algorithms and tests using RooUnfold", in *Proceedings of the PHYSTAT 2011 Workshop, CERN, Geneva, Switzerland, January 2011, CERN-2011-006, pp 313-318*, pp. 313–318. 2011. arXiv:1105.1160.

[41] R. Brun and F. Rademakers, "ROOT: An object oriented data analysis framework", *Nucl. Instrum. Meth.* **A389** (1997) 81–86, doi:10.1016/S0168-9002(97)00048-X.

[42] B. H. Alver, C. Gombeaud, M. Luzum, and J.-Y. Ollitrault, "Triangular flow in hydrodynamics and transport theory", *Phys. Rev.* **C82** (2010) 034913, doi:10.1103/PhysRevC.82.034913, arXiv:1007.5469.

[43] B. Schenke, S. Jeon, and C. Gale, "Elliptic and Triangular Flow in Event-by-Event D=3+1 Viscous Hydrodynamics", *Phys. Rev. Lett.* **106** (2011) 042301, doi:10.1103/PhysRevLett.106.042301.

[44] Z. Qiu, C. Shen, and U. W. Heinz, "Hydrodynamic elliptic and triangular flow in Pb-Pb collisions at $\sqrt{s_{\rm NN}}$=2.76ATeV", *Phys. Lett. B* **707** (2012) 151, doi:10.1016/j.physletb.2011.12.041, arXiv:1110.3033.

[45] L. Yan, J.-Y. Ollitrault, and A. M. Poskanzer, "Universal parameterization of initial-state fluctuations and its applications to event-by-event anisotropy", *Nucl. Phys.* **A931** (2014) 1007–1011, doi:10.1016/j.nuclphysa.2014.09.021, arXiv:1408.0709.

[46] L. Yan, J.-Y. Ollitrault, and A. M. Poskanzer, "Azimuthal Anisotropy Distributions in High-Energy Collisions", *Phys. Lett. B* **742** (2015) 290, doi:10.1016/j.physletb.2015.01.039, arXiv:1408.0921.